Physics of Fluids

Experimental analysis of shock smoothing design strategy for reducing cavitation erosion aggressiveness

Cite as: Phys. Fluids **35**, 013331 (2023); https://doi.org/10.1063/5.0131967
Submitted: 25 October 2022 • Accepted: 30 December 2022 • Accepted Manuscript Online: 01 January 2023 • Published Online: 18 January 2023
Published open access through an agreement with JISC Collections

Jeremy Nahon, Mehrdad Zangeneh, Tomoki Tsuneda, et al.

Physics of Fluids ARTICLE scitation.org/journal/phf

Experimental analysis of shock smoothing design strategy for reducing cavitation erosion aggressiveness

Cite as: Phys. Fluids **35**, 013331 (2023); doi: 10.1063/5.0131967
Submitted: 25 October 2022 · Accepted: 30 December 2022 ·
Published Online: 18 January 2023

Jeremy Nahon,[1,a)] Mehrdad Zangeneh,[1] Tomoki Tsuneda,[2] Motohiko Nohmi,[2] Hiroyoshi Watanabe,[2] and Akira Goto[2]

AFFILIATIONS

[1]Department of Mechanical Engineering, University College London, London WC1E 7JE, United Kingdom
[2]Ebara Corporation, 4-2-1 Honfujisawa, Fujisawa-shi, Kanagawa 251-8502, Japan

Note: This paper is part of the special topic, Cavitation.
[a)]**Author to whom correspondence should be addressed:** nahonjeremy@gmail.com

ABSTRACT

This article presents the experimental analysis of cavitation erosion for two cascade hydrofoil profiles. The aim is to evaluate the change in erosive intensity between a conventional smooth blade surface and one generated by the means of inverse design specifically to reduce cavitation aggressiveness. The applied design strategy consists in imposing a reduced amplitude and gradient at the cavity closure pressure jump in order to bring down the potential energy contained in the vapor sheet. The result is a unique geometry that presents a surface kink located at cavity closure, which successfully smoothes the pressure jump according to computational fluid dynamics (CFD) verification analysis. Here, an experimental rig is constructed and equipped with a pressure sensing system and high-speed imaging to capture the flow field. The measurements for both geometries are first compared against a set of steady-state CFD solutions, which demonstrate the reliability of the inverse design solver for generating targeted flow characteristics in non-cavitating and cavitating conditions. Visual recordings also reveal significant changes in the aspect of the vapor sheet between the two blades indicating a shift in its dynamic behavior. Erosion intensity levels are then measured by paint method at identical conditions. The outcome of the experiment is highly conclusive as a marked reduction in paint erosion is observed for the design geometry. The measured data also serve as a benchmark test for predictive cavitation erosion models by comparing the measured erosion distributions for each blade to those obtained numerically from unsteady CFD.

I. INTRODUCTION

A consequence of pump miniaturization is the intensification of adverse cavitation effects. This includes erosion, which will occur at accelerated rates and downgrade the life expectancy of rotating parts. Current practices for the design of hydraulic machines focus on delaying the initiation of cavitation and on improving the head or power breakdown performance. The problem is that the design choices required for this type of improvement result in a reduction in efficiency. This trade-off between efficiency and cavitation performance is well demonstrated in the work of Bonaiuti *et al.* (2010), who use a three-dimensional (3D) inverse design method to carry out a parametric study on the impact of blade loading on cavitation. They showed that the type of geometry that improves suction performance reduces efficiency. These results are also confirmed by the work of Gulich (2010), Yu *et al.* (2012), Hofmann *et al.* (2001) and Nahon *et al.* (2019). In the long term, the adverse effects that come with delaying cavitation cancel out the gains in cost and performance delivered by the reduced size stage, such that, in order to ensure the viability of the compacting strategy, specific anti-erosion solutions are necessary. In this paper, we present a novel approach in which the hydraulic machine is designed in the presence of cavitation but targets the reduction of cavitation's erosive power.

Experimental studies on cavitation have shown that the intensity of erosion is driven by intrinsic features of the cavity structure, notably shape, unsteadiness, and noise Avellan and Dupont (1988); Chan (1990); Dular *et al.* (2004); Petkovšek and Dular (2013). In Nahon *et al.* (2021), the present authors exploit the aforementioned dependency of erosion intensity on cavity features to devise a strategy for reducing erosive power. The methodology is centered on the principle

that the steeper the rates of variation of ambient pressure in time and space are, the more aggressive potential bubble collapses will be on solid surfaces (Brennen, 2013; Hammitt, 1963).

This led to the development of an inverse design algorithm for hydrofoil cascades under cavitating flow (Nahon *et al.*, 2021). The algorithm works by taking a loading distribution as input from the user and solving the combined computational fluid dynamics (CFD)-geometry problem to generate a blade geometry and a flow field that match the prescribed conditions (Zangeneh *et al.*, 1996; Bonaiuti *et al.*, 2010; Tiow *et al.*, 2002). In our inverse design technique, the loading is defined as the difference in pressure Δp between blade pressure and suction sides and it is imposed during computation by treating the blade surfaces as permeable walls. The blade shape is then updated at every iteration by solving the flow tangency ordinary differential equation (ODE) until holistic convergence for both the geometry and the flow field is attained. Figure 1 provides a schematic workflow of the inverse design procedure. To enable the prediction of cavitating flow, the Tohoku–Ebara equation of state is incorporated into the CFD formulation, Nohmi *et al.* (2003). It treats cavitating water as a homogeneous compressible mixture wherein density is dependent on static pressure and it takes into account air presence in the mixture.

The study presented in Nahon *et al.* (2021) produced a pair of blade profiles: (i) a baseline blade with a conventional high-amplitude, high gradient pressure jump, (ii) a redesigned blade obtained by imposing a smooth pressure rise at cavity closure to theoretically reduce bubble collapse aggressiveness. Both are designed such that hydrodynamic performance; that is, pressure rise and flow turning are

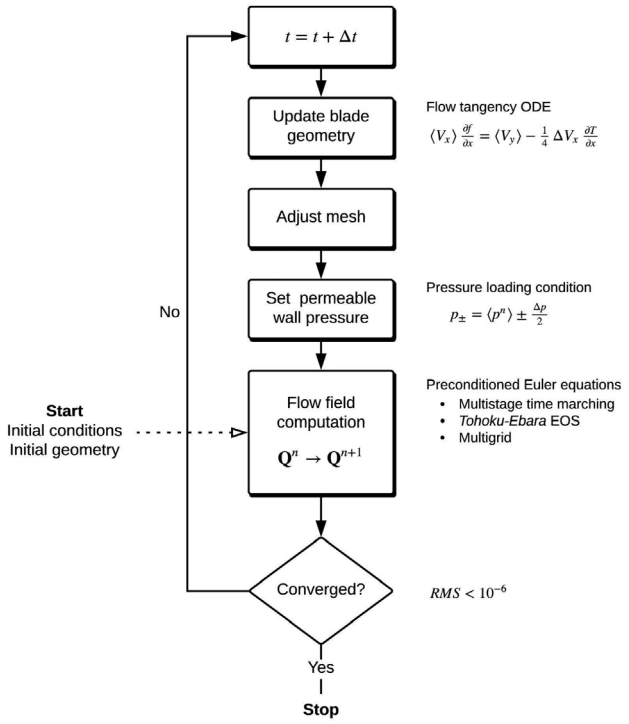

FIG. 1. Algorithmic workflow of the inverse design methodology for cavitating flow (Nahon *et al.*, 2021).

equal across blades, as demonstrated in Nahon (2020). The results were validated numerically using both in-house and commercial solvers to show the change in blade pressure, but the improvement in erosive performance could not be demonstrated. This is the objective of the analysis presented here, which provides an experimental comparison of the two geometries to demonstrate the change in erosive intensity. The experiment is carried out in two stages: (i) a cavitation characterization analysis aimed at capturing the features of blade cavity for both geometries and (ii) a comparative erosive intensity evaluation. For the latter, we adopt the painted surface method to accelerate the observation of material degradation (Fukaya *et al.*, 2010; Li *et al.*, 2014).

This paper also presents a numerical study of cavitation erosion for the two geometries, complementing the experimental findings. Erosive aggressiveness predictions are obtained through time-resolved CFD analysis of the cavitating flow field combined with competing approaches for erosion prediction. Two bubble-scale mechanisms are thought to cause material deformation and removal: (i) micro-jets and (ii) collapse pressure waves. Some research suggests that the pressure wave is substantially dampened by the liquid and only contributes to imploding near-surface bubbles and generating micro-jets (Blake, 1988; Lohrberg, 2001; Dular *et al.*, 2006; Shimada *et al.*, 1999; Peters *et al.*, 2015; Sagar and el Moctar, 2020). Concurrently, others ascribe cavitation erosion entirely to the cloud collapse pressure wave (Avellan and Dupont, 1988; Pereira *et al.*, 1998; Fortes Patella and Reboud, 1998; Kato *et al.*, 1996; Li *et al.*, 2014; Ochiai *et al.*, 2010). Here, we have chosen to compare four prediction models: Peters *et al.* (2015), Li *et al.* (2014), Mouvanal *et al.* (2018), and Nohmi *et al.* (2009), which cover both causal interpretations (see Table I).

The present paper begins by detailing the two competing geometry profiles. Experimental platform and protocol are then described, before we lay out and discuss the results for the cavitation characterization first and the erosion analysis second. Finally, erosion data are processed and compared to the numerical aggressiveness results.

II. CASCADE GEOMETRIES

The two compared geometries are results of the design study presented in Nahon *et al.* (2021). The baseline blade comes from an axial pump impeller profile taken at the shroud. It presents a smooth surface which, under cavitating conditions, produces a sharp pressure jump at cavity closure.

The new design was obtained by running the inverse algorithm in identical conditions using a smoothed loading specifically at the closure jump. As a result, the new blade's distinct feature is a surface kink in the affected region and a low-gradient pressure recovery. Hydrodynamic parameters such as lift, drag, and flow turning remain unchanged, meaning that any change in erosion aggressiveness can only be imparted to the change in pressure jump. Pressure profiles in cavitation conditions and blade geometries are shown in Fig. 2.

III. EXPERIMENTAL SETUP

The test section is made up of $N = 6$ stacked channels (five blades plus pressure/suction surfaces to enclose the top/bottom channels). To facilitate construction, the cascade is rotated such that the inflow direction is no longer at $\gamma = 46.321°$ but horizontal, meaning that hydrofoil stacking is slanted at angle γ. The number of channels is selected such that boundary layer effects at the walls do not affect the central

TABLE I. Selected erosion prediction models for the numerical analysis of cavitating flow.

Predictor model	Assumed erosion mechanism	Determining variable
Peters *et al.* (2015)	Micro-jet water hammer	Jet velocity $v_{jet} \propto \sqrt{p - p_v}$
Li *et al.* (2014)	Pressure wave and energy cascade	Pressure change at collapse $\partial p/\partial t$
Mouvanal *et al.* (2018)	Pressure wave and collapse detector	Collapse conditions and pressure p
Nohmi *et al.* (2009)	Pressure wave	Linear combination of time derivatives for pressure and volume fraction

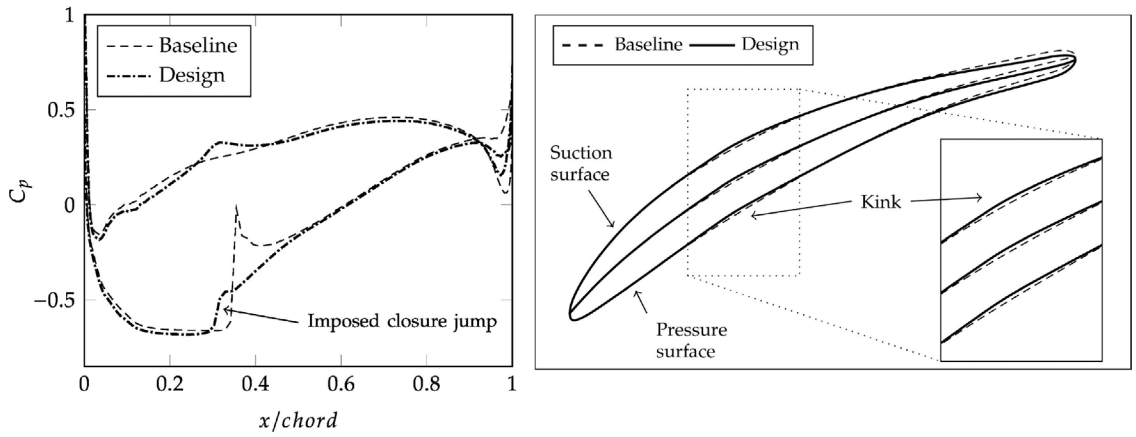

FIG. 2. Comparison between baseline and design blades produced in Nahon *et al.* (2021). The main effect of the loading modification on the shape is in the kink region: (a) blade pressure distribution in cavitation conditions ($\sigma = 0.68$) and (b) full blade geometries.

channel where the measurements are taken. To minimize three-dimensional effects, the span is set equal to the axial chord, that is, 0.09 m. This spanwise distance is sufficiently large to deliver uniform spanwise flow at the hydrofoil mid-section. The flow conditions for the hydrofoil cascade are detailed in Table II.

To be able to swap easily between the two geometries, the blade parts separate from the support frame. Each blade part consists of the extruded profile and the base [see Fig. 3(b)], which fits into a hollowed-out grove in the support wall. The top and bottom cascade walls are also interchangeable and follow the shape of either the suction surface (bottom wall) or pressure surface (top wall).

Downstream of the cascade, the top and bottom trailing walls are mounted on a hinge allowing for angle adjustment. This feature is important as it maintains the periodicity of the outflow by matching the flow and wall angles. The verification is performed before each experimental run by turning the screws installed to that effect (see Fig. 3).

TABLE II. Scaled operating conditions and dimension of the experimental cascade.

Experimental operating conditions	
Inlet velocity	14.48 m/s
Axial chord	0.09 m
Pitch	0.06 m
Channel number N	6
Span	0.09 m
Cross-sectional area	3.24×10^{-2} m^2
Volume flow rate	19.44 m^3/min
Reynolds number Re	1.3×10^6

The cascade casing connects to the inlet and outlet ducts. A honeycomb structure is fitted into the inlet pipe to enforce a uniform horizontal inflow. The casing is equipped with an observation window through which cavitation and trailing wall angles are monitored. To suppress tip leakage, 2-mm-thick silicon membranes, cropped to the shape of the blade profiles, are attached to the top of the blade pieces. The complete testing platform is shown in Fig. 4.

A. Control and measurement system

Volume flow rate is measured downstream of the test section using an electromagnetic flowmeter. Fluid temperature is measured at the tank. Friction causes water to heat up during experimentation. This effect is taken into account in the calculation of the cavitation number σ by taking the value given by the Tetens equation for the saturation vapor pressure (Monteith and Unsworth (2013)):

$$p_v = 0.610\,78 \exp\left(\frac{17.27T}{T + 273.3}\right), \quad (1)$$

where T is in °C and pv in kPa. To maintain an acceptable temperature around $T = 20 \pm 2$ °C, the tank water is cooled down intermittently.

At the inlet (upstream of the cascade), five pressure taps are holed into the support wall at the pitchwise center of channels 2 to 6. These serve to control periodicity. The same goes for the outlet where six

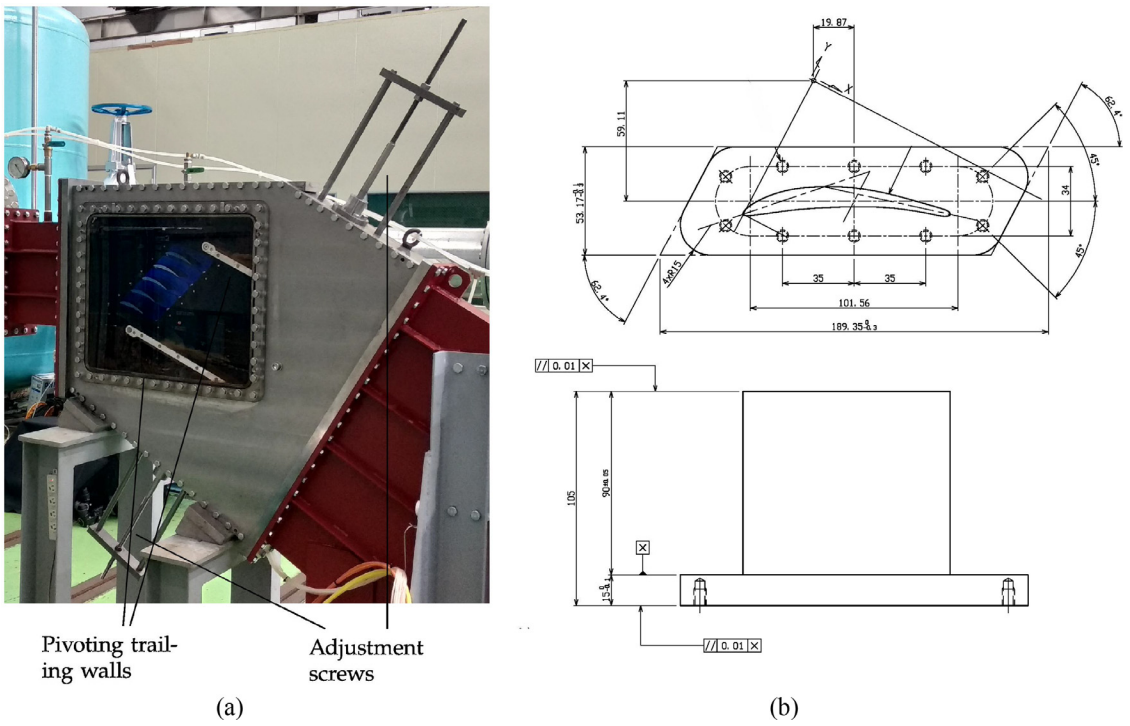

FIG. 3. Cascade section (a) with adjustable trailing walls and observation window. Blade element (b) consisting of the base (constant shape) and the foil surfaces, which vary with the design. (a) Cascade section and (b) removable blade element.

pressure taps are located at the center of all six channels (see Fig. 5). Periodicity is successfully attained when the pressure is uniform across the inlet and the outlet (±2% from average). To record blade surface pressure, nine taps are arranged along the mid-span meridional line on suction side of blade 3 and pressure side of blade 4 (see Fig. 5). For the characterization experiment, every single run—that is one cavitation number and one geometry—happens over a prolonged period of time allowing steady state behavior to establish itself; that is, cavitation cycles are regularly spaced in time and pressure fluctuations are within ±0.2 kPa. Pressure measurements at each location are then taken over a 30 s window at 0.1-s intervals and averaged over that period. This means that statistical fluctuations are incorporated into the measurements presented in this paper.

B. Erosive power assessment configuration

For the erosion assessment experiment, the two center blades with pressure holes are discarded and replaced by even surface blades. The hydrofoils are brush coated uniformly using ethyl acetate-based blue dye at a thickness of 0.005 mm (see Fukaya, 2010) and assembled into the cascade rig. The blades are exposed for a predefined amount of time to constant σ cavitating flow.

IV. CAVITATING FLOW CHARACTERIZATION EXPERIMENT

Here, visual recordings of sheet cavitation and measurements of blade surface pressure are taken for both blade geometries, the objective being to observe their differences. Experiments are run at descending cavitation numbers to follow the growth of the cavity. The inflow pressure measured upstream of channel 4, p_{in}, is used to compute the cavitation number $\sigma = (p_{in} - p_v/(0.5\rho V^2)$ with p_v given by the Tetens equation [Eq. (1)]. Inflow pressure level is adjusted by tuning pump RPM and valve opening of the water circuit. For all pressure measurements, the value is recorded after time has been allowed for sensor stabilization, and the pressure is then acquired over a 10-s window. The difference in height between the tap and sensor, which exerts additional hydrostatic pressure, is subtracted from the sensor reading.

Pressure measurements and cavity length are compared against steady-state numerical solutions obtained from two codes:

1. the In-house solver presented in Nahon *et al.* (2021) based on the Tohoku–Ebara barotropic equation for cavitation modeling (Nohmi *et al.*, 2003) and an explicit preconditioned scheme with upwind SLAU fluxing (Shima and Kitamura, 2011),
2. the Fluent commercial suite using the Zwart–Gerber–Belamri transport model (Zwart *et al.*, 2004) and scalable $k - \varepsilon$ turbulence.

Video data for sheet cavitation are taken at frame rates ranging from 1000 to 40 000 fps. To avoid light reverberating from the aluminum surfaces and masking the vapor region, a thin layer of black paint is applied to all cascade surfaces.

Before the experiment is initiated, the water circuit is de-aired. Preliminary runs revealed large amounts of non-condensable air in the form of visible bubbles entrained with the liquid flow. The issue with preexisting air bubbles is that they expand more rapidly than

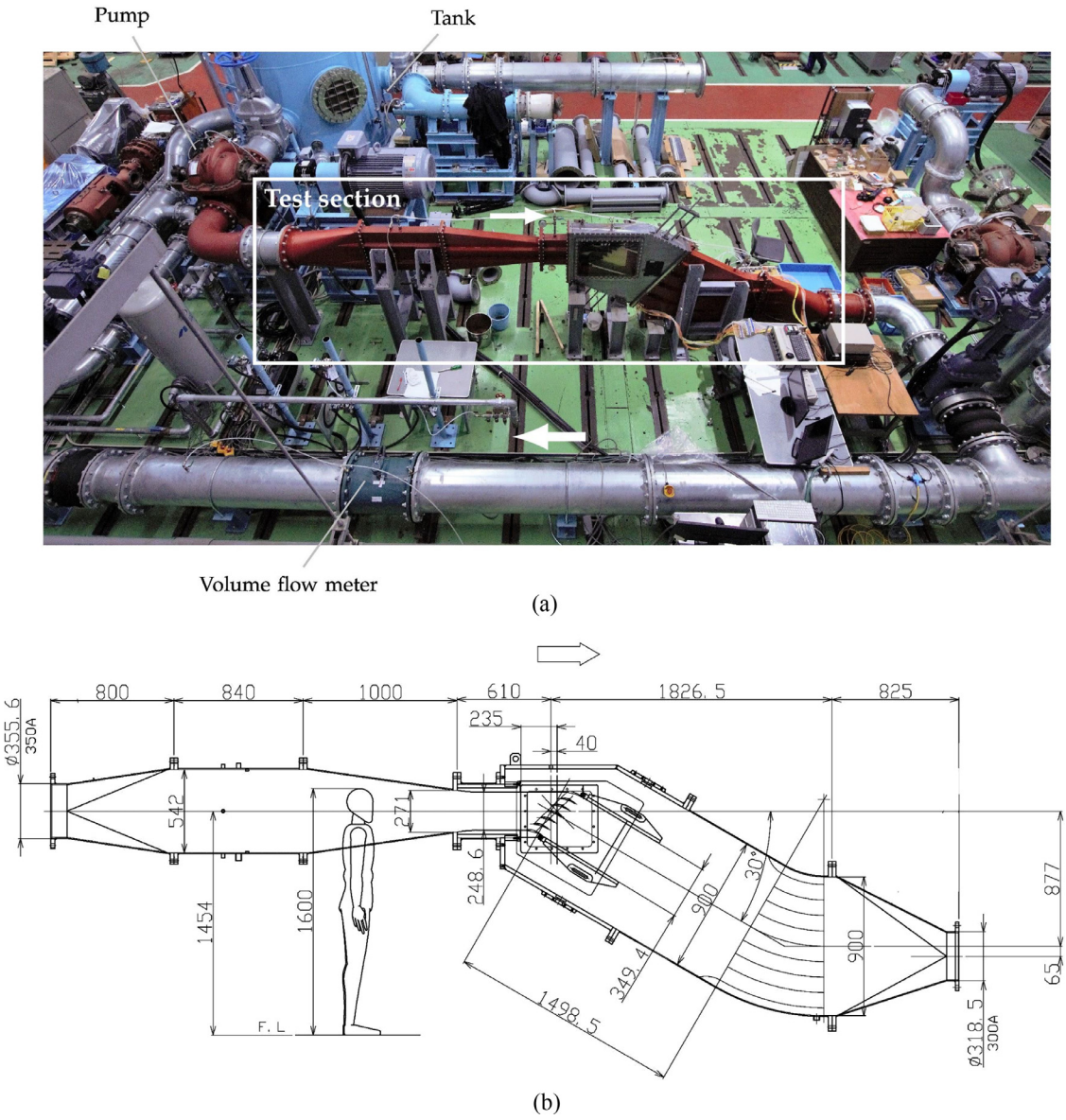

FIG. 4. Experimental installation. (a) Overhead view of water circuit. Circulation in clockwise direction. (b) Test section side view.

vapor bubbles and give the false impression of early cavitation inception. The de-airing process, carried out at regular intervals throughout the experiment, consists of creating a vacuum inside the water tank to suck the absorbed air out of the liquid. Dissolved oxygen (DO) values are kept track of throughout the experiment.

It is important to note that fully removing dissolved air using a deaerator system would create an environment, which does not match the conditions typically found in industry where no effort is made to deaerate liquid flows. For this research, fully de-aerating would bring no added value; on the contrary, we consider it more interesting to observe the differences in cavitation behavior and erosive power in near real conditions.

A. Non-cavitating flow results

Pressure measurements in non-cavitating conditions are shown in Fig. 6 and compared against numerical solutions obtained from the In-house solver presented in Nahon *et al.* (2021) and Fluent. Experimental and numerical results are in good agreement. The small negative offset on the baseline suction side comes from slightly high inflow speed. As expected, the trailing-edge behavior is in closer agreement with the Fluent Reynolds Averaged Navier Stokes (RANS) result than with the In-house inviscid solution. This preliminary non-cavitating result is important because it demonstrates the reliability of the rig, which properly suppresses three-dimensional effects such that experimental flow at mid-span accurately replicates the two-dimensional (2D) cascade flow.

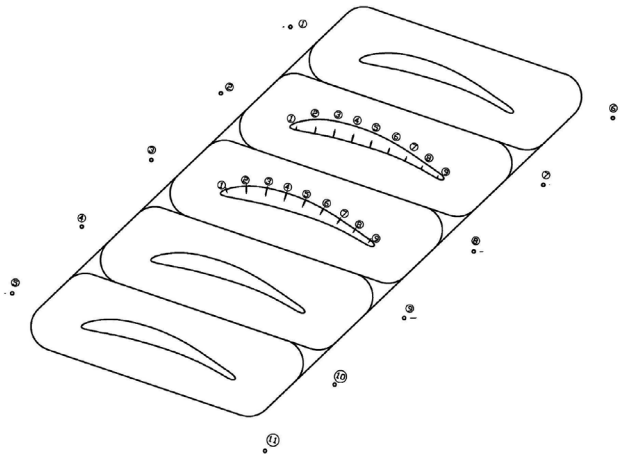

FIG. 5. Placement of pressure taps inside the cascade section used to measure operating conditions and surface pressure. All connect to the pressure sensor through the switchboard.

B. Cavitation flow results

The vapor sheet is first observed around cavitation number $\sigma = 0.87$ for both blades (see image data in Figs. 7 and 8). At this point, the cavity is thin and stable: the closure position does not fluctuate and no shedding is observed. The cavity extends from $x/chord \approx 0.1$ to $x/chord \approx 0.3$. Because of the small thickness of the vapor sheet, the channel choking effect is weak and the closure pressure jump measured between taps 3 and 4 is small. We note that the pressure measured at suction side tap number 4 for the design case consistently coincides with the trough of the wavy pressure distribution as long as it is not covered by vapor ($\sigma > 0.8$).

As the cavitation number diminishes, the vapor sheet stretches further downstream. The upstream portion of the vapor sheet shows a smooth and glassy surface. Toward the closure region, the interface between liquid and vapor is not as well marked: the two independent homogeneous media turn into a heterogeneous mixture characterized by high unsteadiness (see white cavity region in Fig. 7). The thickness and instability of the bubbly region increases as the cavitation number goes down. At $\sigma = 0.66$, vapor structures can reach the trailing edge region before breaking off as the reentrant jet clips the cavity. The vapor structures shed from the cavity sheet correspond to the horseshoe type vortex cloud observed over hydrofoil profiles (Li *et al.* (2014)). As the cavity increases in size, differences between the two geometries are observed. The increase in thickness, for instance, is not as pronounced for the design case as it is for the baseline (see results at $\sigma = 0.73$ or at $\sigma = 0.66$ in Figs. 7 and 8). Most noticeable is the significant shrinking of the bubbly region. At $\sigma = 0.73$, the vapor sheet of the design case remains fully attached from initiation point to closure and the smooth glassy texture appears to cover the entire cavity (Fig. 8). Even at lower cavitation numbers, the majority of the cavity retains a visibly smooth texture, while bubbly flow is limited to the closure and to the downstream region where vapor bubbles are shed. By comparison, the flow around the cavity for the baseline case turns heterogeneous as early as $\sigma = 0.8$ with vortical structures forcing the cavity to detach (Fig. 7).

Inside the cavity, the pressure remains substantially higher than the saturation pressure: approximately 10 kPa instead of $p_v \approx 2340$ Pa at all cavitation numbers. The discrepancy is due to the presence of noncondensable gas in the main cascade flow. Despite the de-airing procedure undertaken before experimental startup, air remains not only under the form of bubbles of varying sizes, which can be observed as they are convected by the flow, but also as dissolved gas in water. To quantify the dissolved oxygen (DO), measurements are taken before each run and values are found to range from 2.3 to 2.8 mg l^{-1}. In low-pressure regions, the air bubbles expand and coalesce with other bubbles to form a visible cavity. The pressure measured in that region is the sum of the partial vapor pressure and partial air pressure. Based on the measurement discrepancy, the latter is estimated at a value of about 7 to 8 kPa.

The pressure measurements give an indication of the gradual rise in sharpness and amplitude of the closure jump. However, evaluating

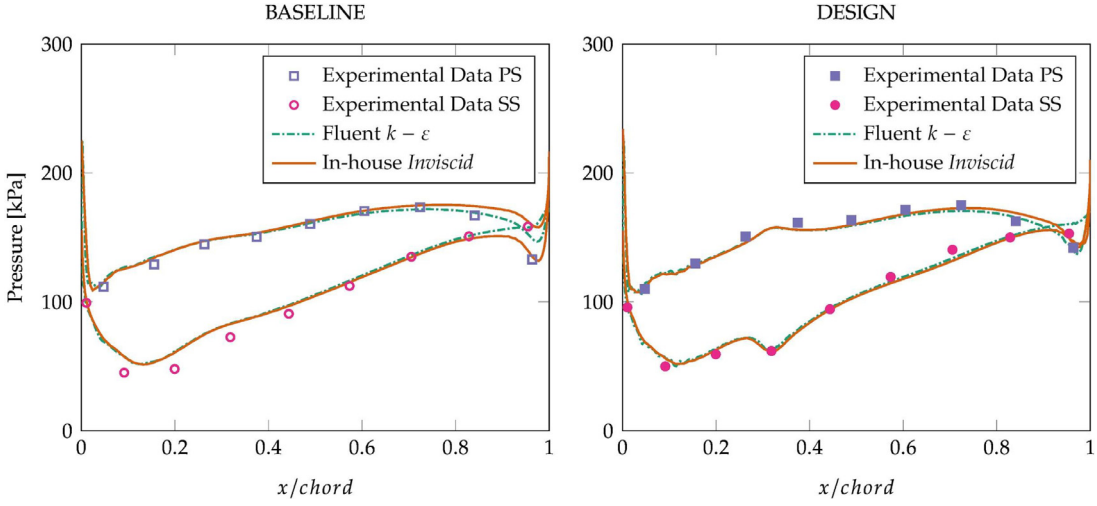

FIG. 6. Non-cavitating absolute pressure measured and calculated at the blade surfaces for the baseline and design cases in non-cavitating conditions ($\sigma = 1.167$).

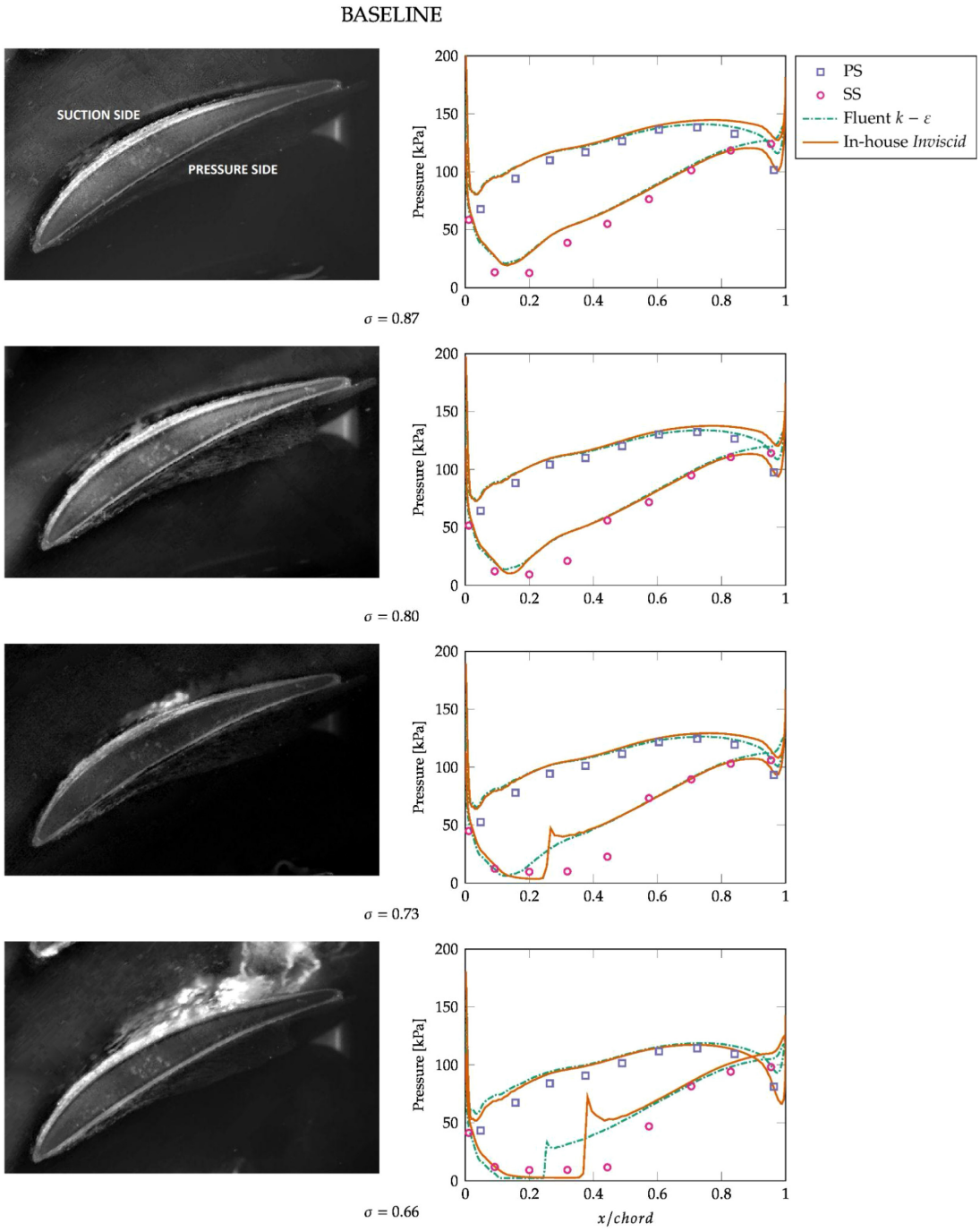

FIG. 7. Baseline geometry cavity recordings shown side by side with measured and calculated pressure values for decreasing cavitation numbers.

the precise location and gradient of the closure shock remains difficult given the limited number of pressure taps. Furthermore, the unsteadiness of the cavity means that the taps in the closure region are covered by liquid and vapor phases in quick succession causing the readings to fluctuate. This applies to, for example, taps number 5 ($x_5/chord = 0.44$) at $\sigma = 0.73$ and number 6 ($x_6/chord = 0.57$) at $\sigma = 0.66$ (see Figs. 7 and 8). A bracket plot for the cavity closure position is plotted in Fig. 9 for all tested cavitation numbers. The minimum and maximum of the bracket bars correspond to the positions of the upstream and downstream taps that enclose the cavity closure. Due to the inherently fluctuating closure position, it is impossible to give an exact location other than the region that comprises it (e.g., $x_5 \leq x_{closure} \leq x_6$ for $\sigma = 0.663$).

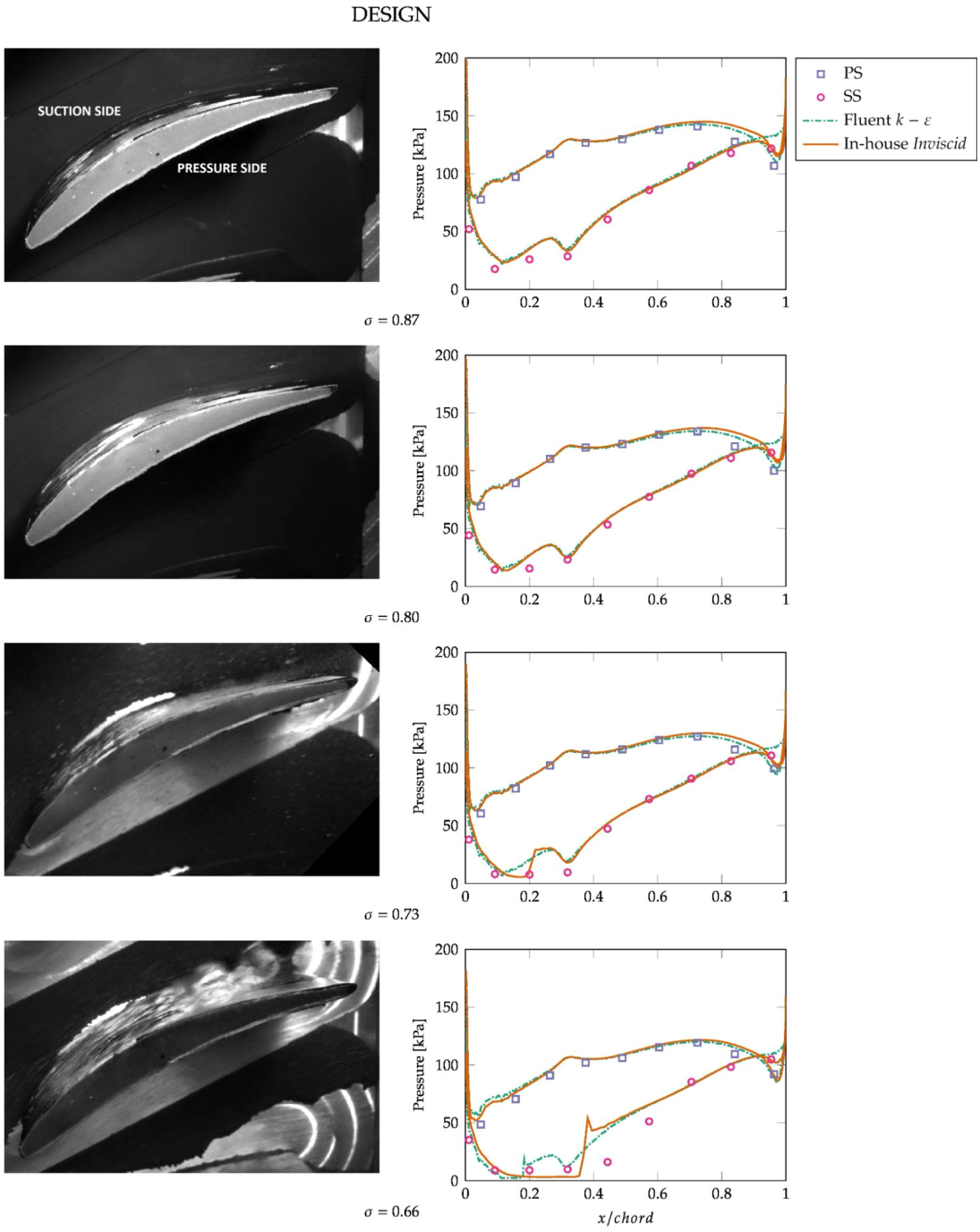

FIG. 8. Design geometry cavity recordings shown side by side with measured and calculated pressure values for decreasing cavitation numbers.

To complement the bracket, an approximate closure point is given by carrying out a cubic spline interpolation of the pressure readings and assuming that the closure point corresponds to pressure crossing the 12 kPa mark. We observe a slower cavity growth rate for the design case than baseline at cavitation numbers $0.65 \leq \sigma \leq 0.7$ when the closure is near the surface kink at $x/chord = 0.35$ (Fig. 9), indicating that one of the effects of the blade surface kink is to curb the expansion of the cavity.

Of most interest is the comparative behavior of pressure when the cavity closure is around the surface kink of the design geometry,

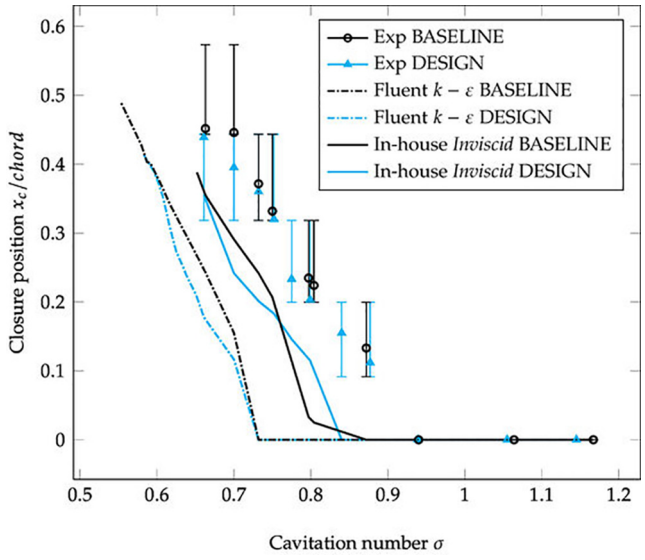

FIG. 9. Measured and calculated closure shock position. For the experimental data, the error bars correspond to the two tap positions upstream and downstream of the closure, and the punctual value comes from the interpolation of the pressure readings and matches the point at which $p > 12$ kPa.

that is, $\sigma = 0.73$ here. For the baseline case, we consider tap number 5—which lies in the unsteady cavitation region—to be pre-closure pressure such that $\Delta p = p_6 - p_5 \approx 50$ kPa. For the design case, it is taps 4 to 5 that bound the closure region and the difference in pressure is 38 kPa. This constitutes a critical observation as it agrees with the theoretical shock softening properties of the design case.

The reduction in pressure jump is at the root of the discrepancies in cavity aspect between the two blades: i. a lower closure pressure means a lesser likelihood of cavity detachment; ii. a softer pressure gradient, acting through baroclinic torque, minimizes vorticity levels; iii. single bubble fluctuation amplitude, driven by the ambient to bubble pressure difference, is minimized. The implication is that, as intended, the design produces a visibly softer cavitation sheet. Not only that the fact that the special aspect of the design case cavity, that is, glassy surface with minimal presence of bubbly flow and well attached sheet, is observed not just at $\sigma = 0.73$ but throughout the experimental range such that the softening effect appears to act in a general manner (Fig. 9).

C. Cavity dynamics

Fluctuations in the length of the cavity are examined here (see Figs. 10 and 11). The length of the cavity is defined as the chordwise distance between the start of the vapor sheet and cavity closure where bubbly mixed flow is observed. The location of the cavity sheet's starting point is stable at x/chord = 0.1 for all cavitation numbers. However, the closure end point moves downstream as the cavitation number descends and fluctuates due to the cavity's cyclical behavior. For both blades, the frequency and amplitude of the closure position vary with the cavitation number. For $\sigma > 0.75$, the change in cavity length is negligible. From $\sigma = 0.75$ to $\sigma = 0.70$, variations increase but the amplitude remains marginal at less than $0.1 \times chord$. The fluctuation cycle occurs at a regular pace with a duration of 5×10^{-3} to 10×10^{-3} s or a frequency in the range 100–200 Hz. Below $\sigma = 0.70$, cavity unsteadiness intensifies: the change in length reaches $0.3 \times chord$, bubbles are periodically emitted from the cavity, and the duration of single oscillatory cycles is prolonged to 20 to 25 s or a frequency around 40 to 50 Hz.

These numbers reveal two dynamic regimes: high and low frequency. The first corresponds to small cavity movements limited to the vicinity of the closure region and occurring at frequencies above 100 Hz. This type of cavitation behavior is observed for $\sigma = 0.75$ to 0.7. The second regime, which applies to cavitation numbers $\sigma < 0.70$, is marked by a drop in frequency to values below 30 Hz and by larger variation amplitudes in cavity volume.

For the baseline case, the increase in unsteadiness follows the decrease in cavitation number. However, for the design case, stabilization in the form of diminished fluctuation amplitude is observed as the cavitation number approaches $\sigma = 0.730$ or when the sheet closure gets near the surface kink. At $\sigma = 0.732$, for instance, the closure displacement is less than $0.1 \times chord$ [Fig. 11(b)]. This reduction in amplitude is observed beyond the design cavitation number. At the lowest pressure run ($\sigma = 0.661$), the cavity does not appear to grow or shrink in length [see Fig. 11(c)]. Instead, changes are observed in the density of bubbles being shed from the frothing closure region. These observations suggest that the features of the design case have stabilizing attributes which activate when the cavity closure is located in the same region as the trough in the suction surface distribution. Here again, the explanation can be traced back to the reduction in shock amplitude: the velocity of the reentrant jet at closure is weakened, minimizing cavity detachment, and, thus, the development of unsteadiness.

D. Performance of numerical schemes

Because of the offset in cavitating pressure, the similarity between the experimental and numerical results in terms of sheet cavitation prediction is downgraded. Both ZGB and TE cavitation models are constructed on the knowledge that phase change occurs for a saturation vapor pressure $p_v = 2339.2$ Pa. Therefore, at the same cavitation number, the numerical solutions deliver a shorter cavity and a reduced pressure jump at closure than the experiment (see Figs. 7 and 8). Performance differences also appear between the two numerical approaches as described in Nahon *et al.* (2021); with the ZGB model, the sheet cavities are shorter and the cavitation number delay is larger. Comparison with the experimental data suggests that the TE model provides a more accurate representation of sheet cavitation as the discrepancy is smaller than with the ZGB solution.

The difference in performance can be accounted for by the treatment of the liquid phase and noncondensable gases. The latter is completely ignored in the ZGB cavitation model (Brennen 2011). The TE Equation Of State (EOS), on the other hand, takes into account the air contained inside the cavitating bubbles, through the air mass fraction parameter Y. The effect is an increase in the compressibility of the mixture. Its value is set at $Y = 1 \times 10 = 5$ for all computations, which matches the order of magnitude of DO in the fluid. The remaining non-negligible offset is explained in part by the fact that Y does not take into account the non-dissolved gases in the form of preexisting bubbles and by the value of the vapor pressure pv, which is a determining parameter in the TE EOS. The observations detailed in

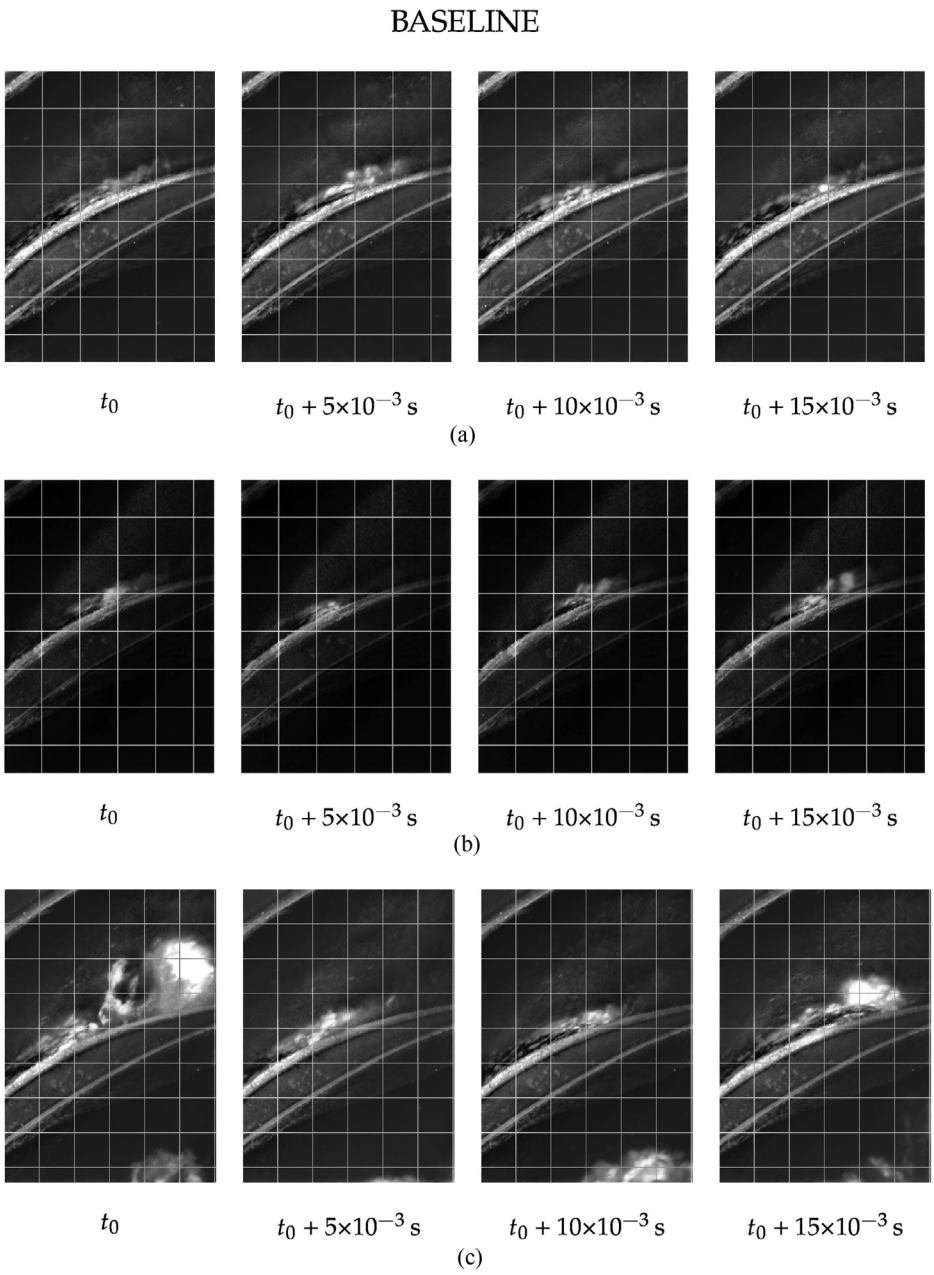

FIG. 10. Baseline geometry cavity variations at decreasing cavitation numbers. Visualizations are single frames of the high-speed recording (at 10 000 fps). Tine t_0 is a time point that complies to two conditions: i. it corresponds to steady state flow behavior and is therefore larger than ramping up time, ii. it marks the start of a cavity sheet cycle. (a) $\sigma = 0.767$, (b) $\sigma = 0.732$, and (c) $\sigma = 0.663$.

Secs. IV A–IV D for both baseline and design geometries are summarized in Table III.

V. EROSION ASSESSMENT EXPERIMENT

The erosion assessment experiment is carried out for the two blade geometries in order to verify the efficacy of the shock smoothing design strategy presented in Nahon *et al.* (2021). Given the flow speeds considered here, it would take close to a hundred hours of operation to obtain detectable material loss for the aluminum cascade. Instead, we opt for the paint removal approach, which accelerates the measurement of erosion aggressiveness.

The assessment is carried out for both baseline and design cases at identical cavitation numbers. Here, $\sigma = 0.73$ is chosen because it corresponds to a cavity closure located at $x/chord = 0.3$ and aligned with the suction side pressure trough for the design case. It is at this condition that the most significant differences are observed with baseline in terms of closure pressure jump and cavity appearance.

In parallel, time-resolved CFD analyses of the baseline and design cavitating cascades are carried out. The erosion results obtained

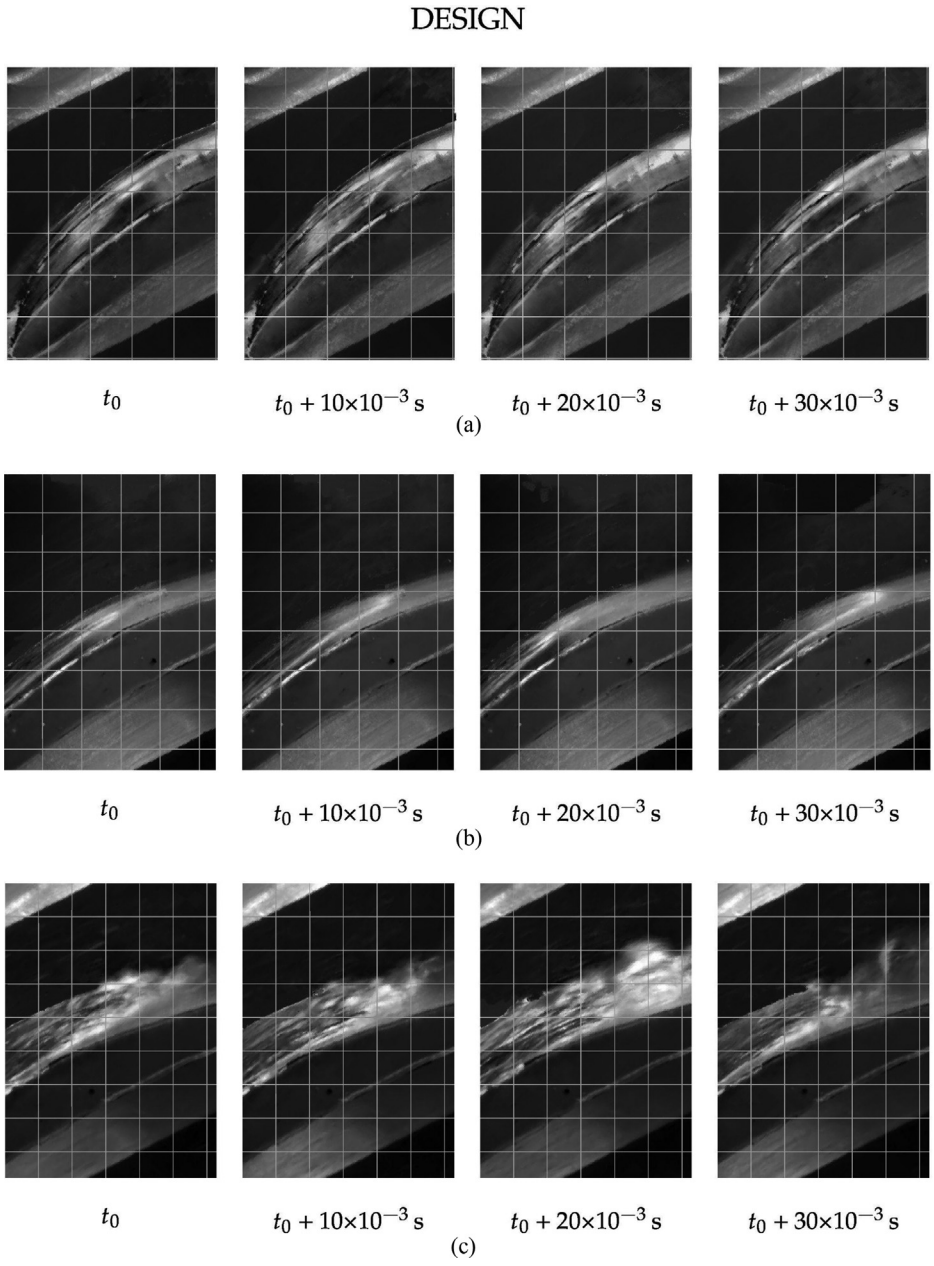

FIG. 11. Design geometry cavity variations at decreasing cavitation numbers. Visualizations are single frames of the high speed recording (at 10 000 fps). Tine t_0 is a time point that complies to two conditions: (i) it corresponds to steady-state flow behavior and is therefore larger than ramping up time, (ii) it marks the start of a cavity sheet cycle. (a) $\sigma = 0.775$, (b) $\sigma = 0.732$, and (c) $\sigma = 0.661$.

experimentally are compared with predictions made numerically. To evaluate the aggressiveness of cavitation erosion from CFD data, four different indicators are implemented:

- Li *et al.* (2014) who use the potential cascade energy of the cavity structure to predict the intensity of the pressure wave:

$$I_{agr}^{Li} = \frac{1}{T}\int_0^T I dt \quad \text{with} \quad I = \begin{cases} \dfrac{\partial p}{\partial t} & \text{if} \quad \dfrac{\partial p}{\partial t} \geq \delta, \\ 0 & \text{if} \quad \dfrac{\partial p}{\partial t} < \delta. \end{cases} \tag{2}$$

- Mouvanal *et al.* (2018)'s detector for critical bubble collapse:

$$I_{agr}^{mouv} = \frac{1}{T}\int_0^T I dt \quad \text{with} \quad I = \begin{cases} p & \text{if conditions are met,} \\ 0 & \text{otherwise.} \end{cases} \tag{3}$$

- Peters *et al.* (2015) who consider that erosion is caused by the micro-jet velocity at bubble collapse:

$$v_{jet} = 8.97\gamma^2 \sqrt{\frac{\rho - \rho v}{Q}}. \tag{4}$$

TABLE III. Summary of observations on the cavitating flow field for baseline and design geometries.

	Observations			
Blade case	Non-cavitating pressure	Cavity shape and texture	Closure pressure jump	Cavity dynamics
Baseline	Smooth (monotonous) distribution on both sides of blade	Thicker with marked heterogeneous interface	Consistently larger jump, $\Delta p \approx 50$ kPa at $\sigma = 0.73$	Transition from high- to low-frequency regime at $\sigma = 0.70$, steady increase in variation amplitude
Design	Wavy pressure profile, most notably on the suction side with a trough at $x/c\ hord = 0.3$	Thinner cavity with glassy interface, length increase slows down near $\sigma = 0.73$ in comparison with baseline	Reduction in pressure jump, $\Delta p = 38$ kPa at $\sigma = 0.73$	Same regime transition point, variation in amplitude stabilizes near $\sigma = 0.73$ and smaller clouds are shed at low σ

- Nohmi *et al.* (2009)'s techniques which combine the pressure and volume fraction and their time derivatives in

$$\frac{1}{T}\int_0^T \alpha \max\left(\frac{\partial p}{\partial t}, 0\right), \tag{5a}$$

$$\frac{1}{T}\int_0^T \alpha \max(\rho - \rho_v, 0), \tag{5b}$$

$$\frac{1}{T}\int_0^T p_\infty \max\left(\left|\frac{\partial p}{\partial t}\right|, 0\right), \tag{5c}$$

$$\frac{1}{T}\int_0^T \max\left(\left|\frac{\partial p}{\partial t}\right|, 0\right). \tag{5d}$$

This experiment is therefore aimed at i. comparing the change in erosive intensity brought by the new design and ii. at evaluating the predictive performance of various numerical indicators for a well-controlled geometry set.

A. Experimental protocol

For the erosion assessment by paint application, the two holed blades are replaced by even surface blades, which have already been spray-painted uniformly. The same procedure carried out for the cavitation characterization experiments is used to adjust the valve opening and pump RPM to get the desired cavitation number. The operating conditions are maintained during exposure time. A preliminary test is run at cavitation numbers $\sigma = 0.75$ to 0.73 (see Table IV) to determine the adequate duration of the erosion test. Using the baseline geometry, it was found that at least 8 h of cavitation exposure are necessary to produce visible patterns. For the comparative study, 15 h of exposure at $\sigma = 0.73$ are chosen as appropriate.

TABLE IV. Run details for the erosion experiments.

Experimental run	Geometry	Test conditions
1 (preliminary)	Baseline	6.4 h at $\sigma = 0.75$, followed by 9 h at $\sigma = 0.73$
2	Baseline	15 h at $\sigma = 0.73$
3	Design	15 h at $\sigma = 0.73$

After exposure, images are taken of the suction surface along the central channel where the flow field is well controlled. The image data are processed to provide a one-dimensional distribution of the erosion intensity along the axial direction. The result is compared to: (i) the experimental erosion distributions obtained for the other tested blade, and (ii) the numerical erosion indicators applied to the time-resolved simulations.

B. Time-resolved CFD procedure

ANSYS Fluent is used with a pressure-based coupled solver for robustness and efficiency, and the Zwart–Gerber–Belamri approach for cavitation modeling. Face values are given by the high-order QUICK scheme, while time integration is achieved through second-order implicit marching with $\Delta t = 5 \times 10 = 5$ s for $CFL \approx 0.3$. All calculations are run for a minimal physical duration of 0.5 s or until the monitored quantities are either constant or fluctuate in a stable manner. We chose a Unsteady Reynolds Averaged Navier Stokes Equation (URANS) $k-\omega$ Shear Stress Transport (SST) approach for its treatment of adverse pressure gradients and separated flows, which are both features of the cavitation closure region. All modeling choices are summarized in Table V.

The computational domain consists of a single cascade channel centered around the blade bounded by periodic boundaries at the top and bottom. Inlet and outlet boundaries are, respectively, placed at $1 \times chord$ and $4 \times chord$ from the leading edge. The mesh is generated using an unstructured quad-dominant topology. A velocity boundary condition is used at the inlet with velocity magnitude and direction fixed at $|V| = 14.48\ \mathrm{m\ s^{-1}}$ and $\gamma = 46.321°$. At the outlet, static pressure is fixed and determines the cavitation number value. Inlet turbulence intensity and turbulent viscosity are set at, respectively, 5% and $\mu t/\mu = 10$. Flow is assumed to be isothermal. The mesh is unstructured and almost exclusively quadrilateral (one single tetrahedral cell at the bottom acute angle of the inlet boundary) with a maximum edge length of $2 \times 10 = 3$ m. The viscous sublayer is resolved with $y^+ \leq 1$ (or $y \approx 1 \times 10 = 6$ m for the present flow conditions and geometry) with 75 cells in the boundary layer. The total cell count exceeds 100 000. The grid topology and cell size are based on the unsteady CFD analysis carried out in Ducoin *et al.* (2012) for 2D hydrofoils.

TABLE V. CFD configuration for unsteady cavitating simulations.

Computational modules	Selected models and details		
Solver schemes	Time discretization	Second-order implicit	$CFL = 0.3$, $\Delta t = 5 \times 10 = 5$ s
	Navier–Stokes discretization	Pressure based	Coupled momentum and continuity equations, QUICK face interpolation
Spatial discretization	Unstructured Quad-dominant	max edge length $= 2 \times 10^{-3}$ m	75 nodes in the boundary layer
Cavitation	Homogeneous mixture	Transport equation	Zwart–Gerber–Belamri in default configuration, $pv = 2339.2$ Pa
Turbulence	RANS	k–ω SST	Resolved boundary layer, $y^+ \leq 1$

The four erosion metrics are evaluated using the time accurate pressure, volume fraction, and mass transfer rates provided by the computation. Following the technique laid out in Nohmi *et al.* (2009), the transient values are taken at the blade surface. The calculation is carried out by running *ad hoc* routines at the post-processing stage. The algorithm interprets the recipes provided by the authors Li *et al.* (2014), Nohmi *et al.* (2009), Peters *et al.* (2015), and Mouvanal *et al.* (2018) and accrues the recorded erosive events over the effective duration of the simulation (eliminating the initial ramping up). The results are normalized over time to get the geometry-dependent erosion rate distribution.

To make the comparison between numerical and experimental results viable, the offset in cavitation inception has to be taken into account. Indeed, running the CFD at $\sigma = 0.73$ would be useless given the discrepancy in cavity length. Instead, it is the closure location found experimentally at $\sigma = 0.73$ that serves as reference, that is, $x/chord = 0.3$. For this numerical study, it was found that runs with an outlet static pressure equal to 108 kPa and $\sigma_{num} = 0.585$ produced the desired cavity length for both geometries.

C. Experimental painted blade results

1. Preliminary case

As shown in Fig. 12, which presents the preliminary test exposure, the eroded zones appear as clusters of paint free specks or as continuous paint-free regions. The density of visible metal determines the intensity of cavitation erosion. Several separate regions are picked up. At the leading edge, the erosion is caused by the impact of solid particles carried by the water onto the surface. The particles are metallic dust or detached fragments of the honeycomb structure contained in the inflow pipe. This type of solid to solid erosion is of no interest to this research. Slightly further downstream, a low-intensity erosion region is visible. In this case, paint removal is caused by cavitation. However, the origin of cavitation is not the drop in surface pressure but low-pressure vortices emanating from particles clinging to the leading edge. As such, this manifestation of erosion is of no value either.

The third larger region located at mid-blade is the erosion action of interest here. Its location matches the sheet cavity closure position. The streamwise spread comes from the change in operating conditions (see Table IV) and the movement of the closure. In the spanwise direction, the eroded zone is not uniformly distributed: the surface is intact close to the walls and the density of metal specks is maximum at mid-span. This agrees with the spanwise shape of the experimental cavity, which disappears at the side walls and flattens between $0.3 \times span$ and $0.7 \times span$. The areas affected by wall effects are eliminated from the study. Instead, the region of analysis is limited in span to the uniform erosion section (see Fig. 12).

2. Comparative erosion analysis

The main comparative erosion tests—that is, baseline and design for 15 h at $\sigma = 0.73$ (see Table IV)—are shown in Fig. 13. The substantial reduction in erosion intensity for the Design case is immediately visible: the paint layer in the region corresponding to cavity closure is

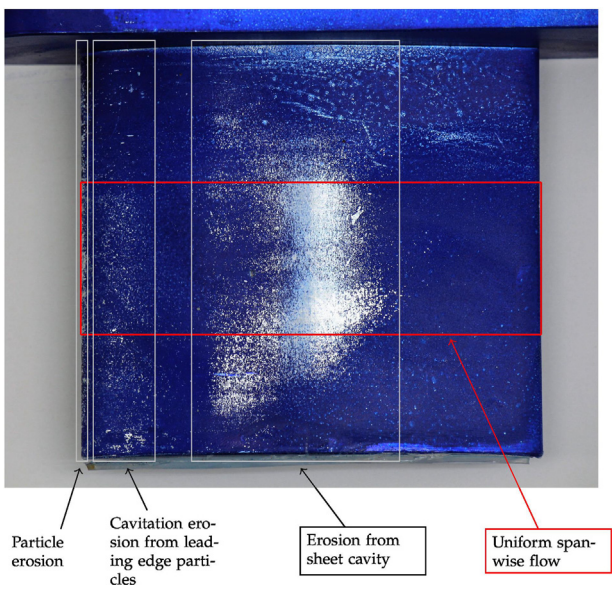

FIG. 12. Paint removal after the preliminary run (number 1 in Table IV: 6.4 h at $\sigma = 0.75$ followed by 9 h at $\sigma = 0.73$). Only the principal erosion region is caused by bubbles collapsing at the sheet cavity closure.

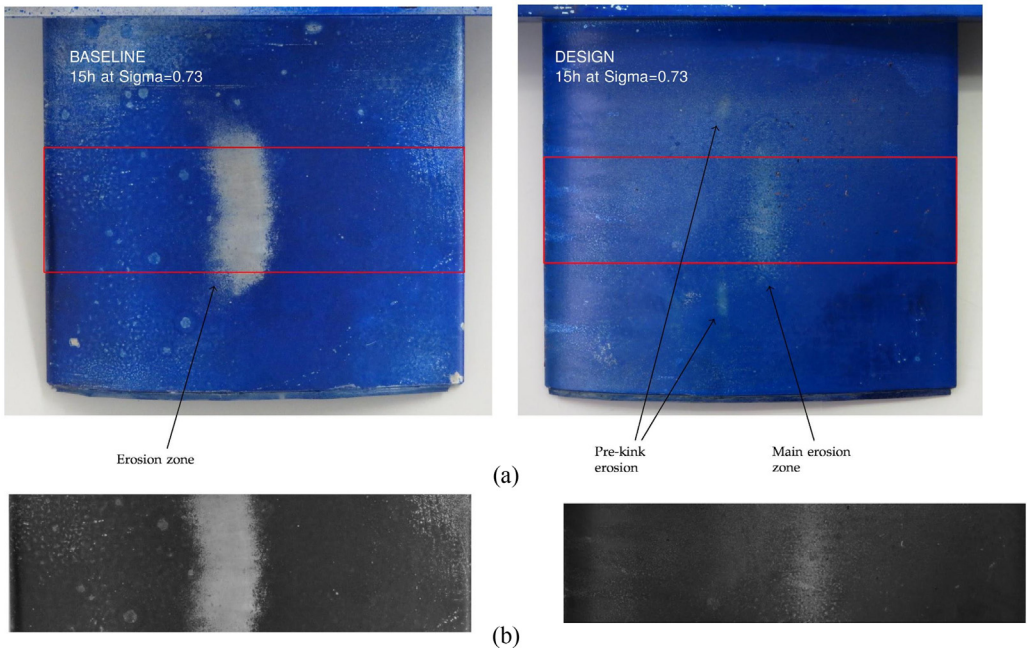

FIG. 13. Paint removal after full test run (15 h at $\sigma = 0.73$) for baseline and design geometries. (a) Full suction surface and (b) cropped to uniform spanwise section and converted to gray scale.

only thinned instead of completely removed for the baseline case. We saw in the characterization experiment that the new geometry produces softer cavitation: the cavity is better attached and the closure region is more homogeneous. The outcome of the erosion test suggests that these attenuated cavitation features are transmitted to the erosion aggressiveness. This constitutes a positive indication of the validity of our shock smoothing design strategy.

Also worth noting for the design case are the small twin erosion zones located upstream and equidistant from midspan. Side-wall effects force the cavity to close further on the other side of the smoothing kink. This position matches the peak in the wavy distribution where the closure jump is amplified rather than attenuated. As a result, erosion is also present at the pre-kink point for the Design case. This supports the correlation between shock amplitude and erosion strength.

The reason why this specific geometry causes erosion to reduce is that it is designed specifically to soften the pressure gradient at cavity closure. This connects to the findings of Hammitt (1963) and Brennen (2013) who relate cavitation aggressiveness to the rate of pressure change exerted on bubbles. This principle is what applies here: vapor

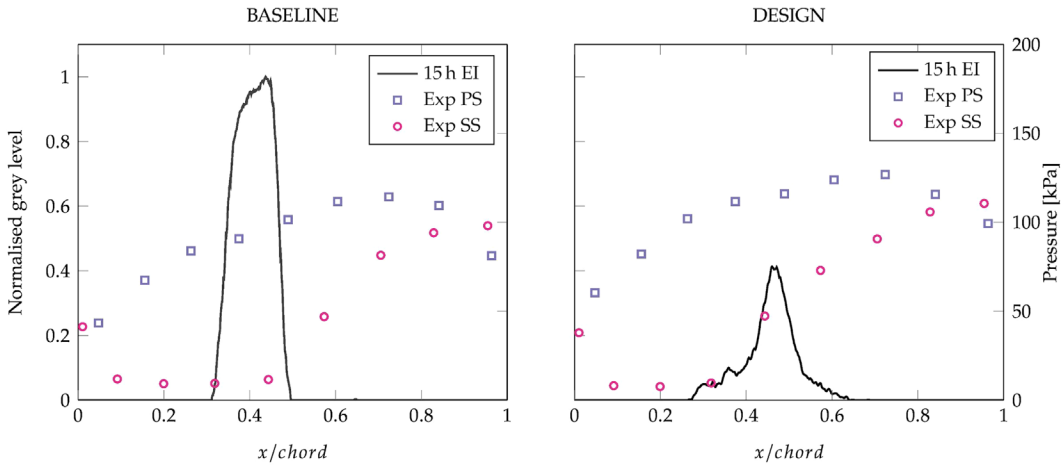

FIG. 14. Streamwise distribution of gray-level erosion indicator [spanwise averaged from Fig. 13(b)] compared against the measured surface pressures at $\sigma = 0.73$.

bubbles travel from a low-pressure region to a high-pressure region; in the case of the baseline blade, the change in pressure is fast causing large-amplitude oscillations at bubble level before collapse, whereas for the design blade, these oscillations are reduced thanks to the slower pressure rise.

It is essential to note that the geometry kink in the design presented here was not produced through empirical know-how or iterative loops but by applying the inverse design technique in conjunction with the known low-pressure gradient low erosion principle. The implication is that this strategy, which manages to reduce erosion without any performance penalties, is universally applicable to all types of bladed machinery where cavitation erosion is a risk.

From the RGB images of the suction surfaces, grayscale conversions are obtained by cropping the center region to eliminate nonuniform spanwise sections [see Fig. 13(b)]. With the color conversion, each pixel carries a scalar value, which determines whether the surface is bare aluminum (lighter) or paint (darker). In this format, the image turns into a two-dimensional matrix where each column and row correspond to fixed streamwise and spanwise positions, respectively, and each value is a measure of the erosive intensity *EI*. The 2D distribution is column-averaged and normalized by the span length of the evaluated section to provide a streamwise erosion profile. Furthermore, because of differences in color tones at image acquisition, all experimental distributions are normalized by the erosion intensity of the fully eroded surface for the baseline test such that a value of 1 represents a paint free zone.

The resulting profiles are shown in Fig. 14 and superimposed on the pressure measurements at $\sigma = 0.73$. For baseline, the principal eroded zone is spread over taps 4 and 5 from $x/chord = 0.3$ to $x/chord = 0.5$, which corresponds to the unsteady downstream part of

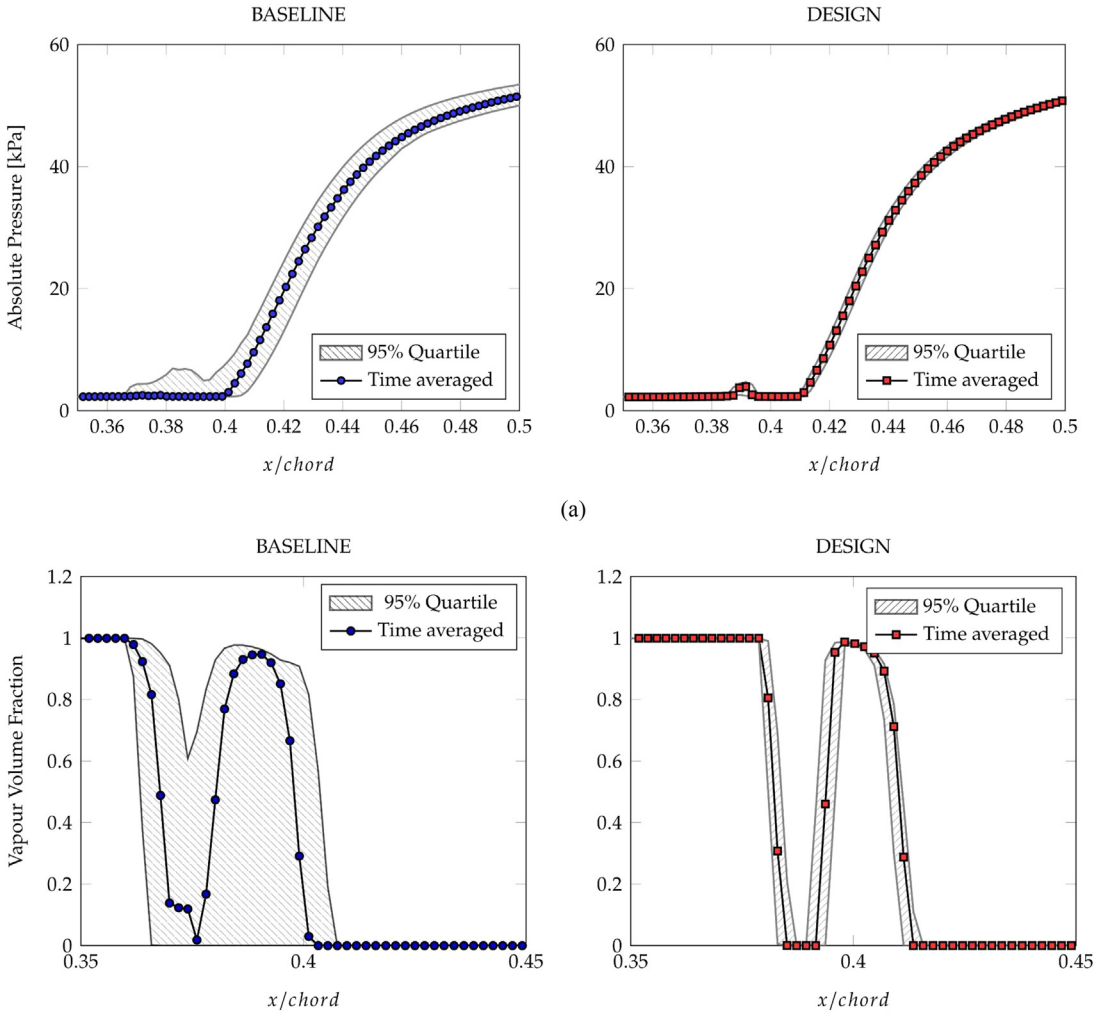

FIG. 15. Unsteady CFD surface pressure and volume fraction for a cavity length equal to $x/chord = 0.4$. The spread contains 95% of the unsteady data. (a) Pressure and (b) volume fraction.

the cavity. The peak in erosion between $x/chord = 0.37$ and $x/chord = 0.46$ is located at the final low-pressure reading. In this zone, the paint layer is fully removed, so it is likely that the real erosive intensity exerted between $x/chord = 0.37$ and $x/chord = 0.46$ onto the aluminum surface is not as flat as presented here.

For the design, the erosion patch is shifted downstream of the baseline one and centered between pressure taps 5 and 6. With the characterization experiment, we saw that the baseline and design cavity lengths were comparable (see Fig. 9). It is therefore advanced that the particular pressure distribution of the design is able to suppress a large number of collapse events between $x/c\ hord = 0.3$ and $x/c\ hord = 0.42$ and only the weaker erosive action occurring between $x/c\ hord = 0.42$ and $x/chord = 0.5$ affects the blade surface.

D. Time-resolved CFD results

In Fig. 15, the pressure and volume fraction distributions on the blade surfaces are plotted at $\sigma_{num} = 0.585$. Both the time-averaged values and spread (95% quartile range) are presented. The variability data inform us on the unsteadiness of the cavity sheet blade pressure. The narrowness of the variability zone for the design case indicates a steadier cavity behavior than baseline. This numerical finding is in line

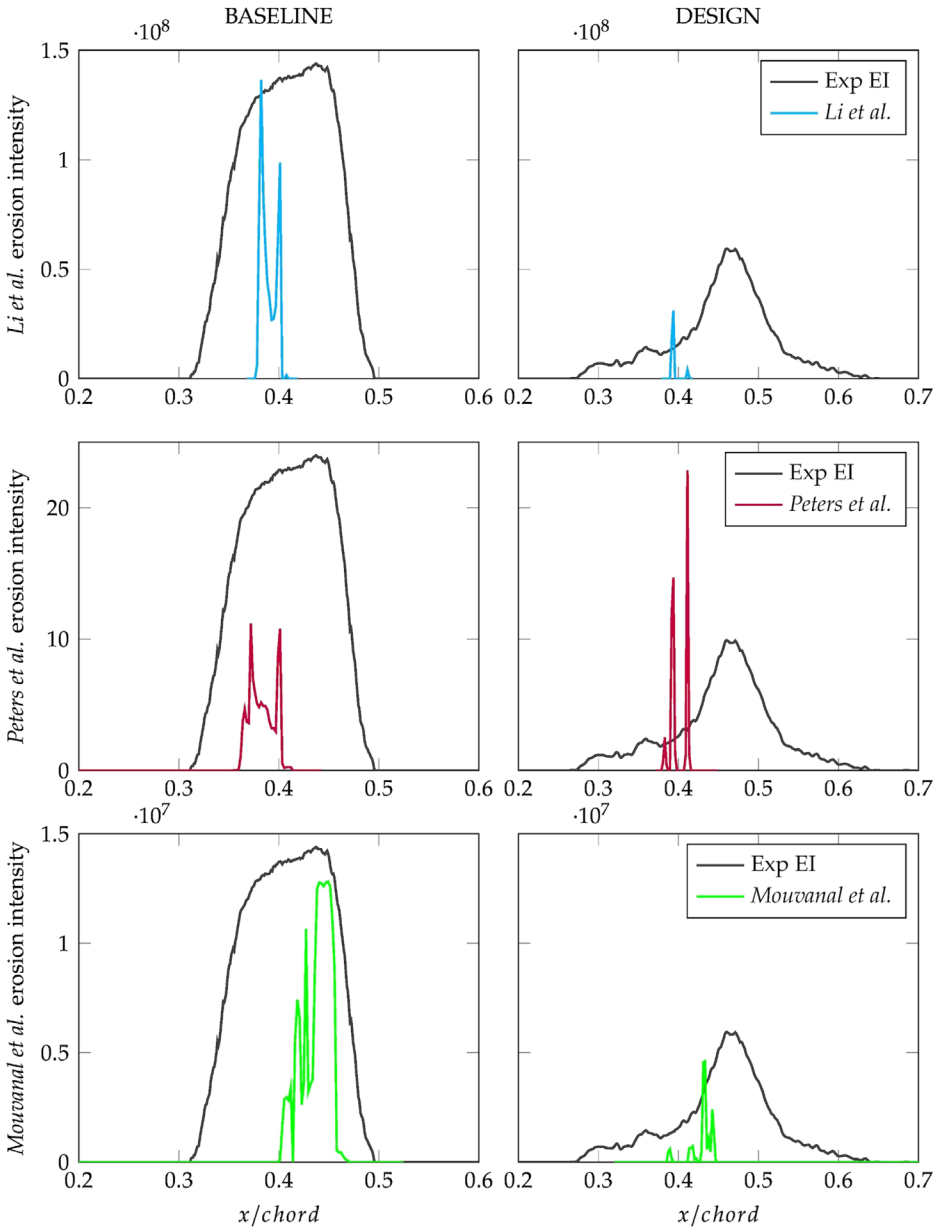

FIG. 16. Comparison of experimental gray level with Li *et al.*, Peters *et al.*, and Mouvanal *et al.* erosion indicators.

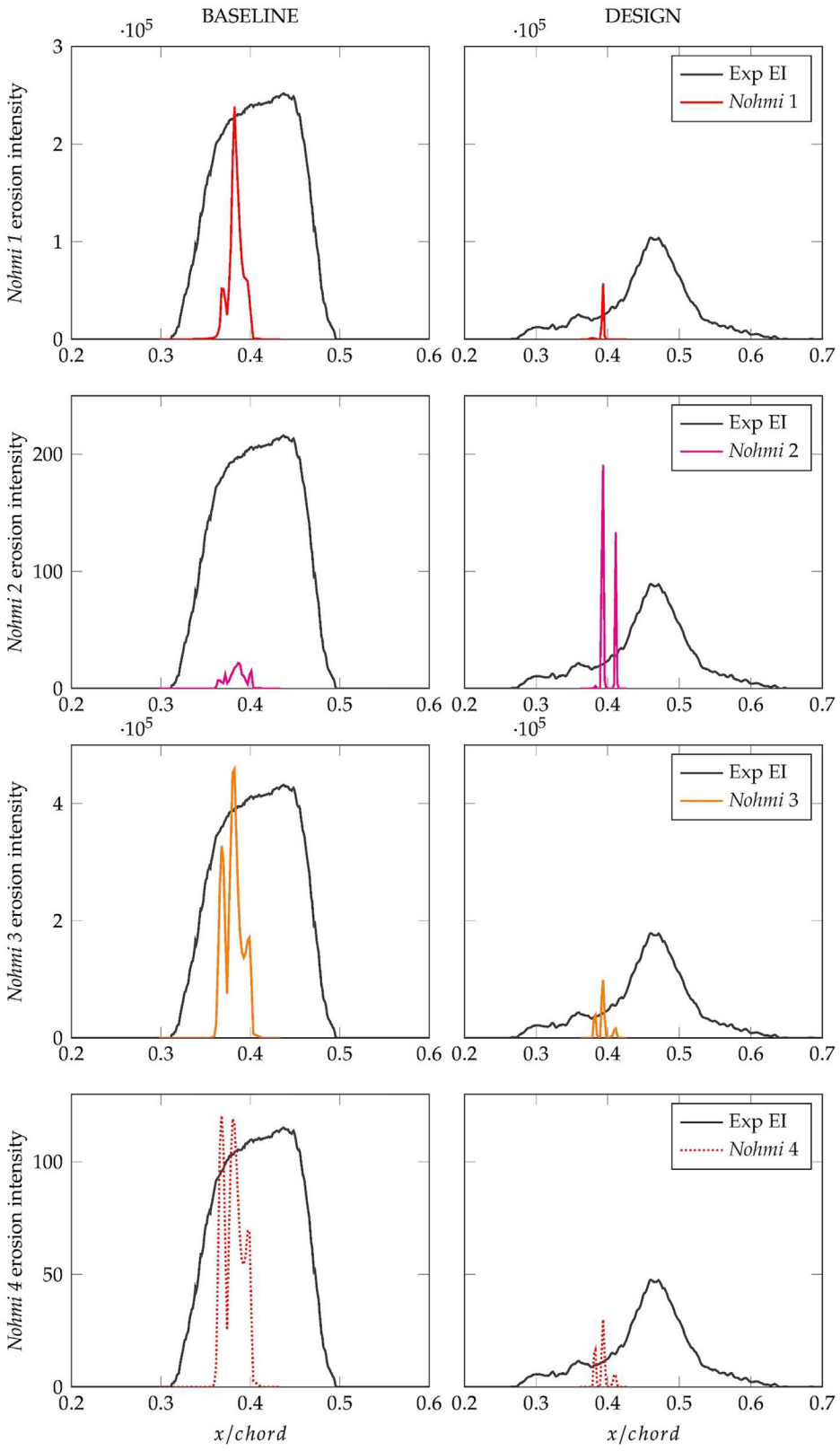

FIG. 17. Comparison of experimental gray level with computational erosion predictions for Nohmi *et al.* indicators.

with the experimental observations of cavity dynamics for both cases (see Figs. 7 and 8).

In Figs. 16 and 17, we compare the experimental erosion distributions for both geometries to the predictions obtained numerically. We are most interested in verifying whether the position of the erosion zone and the intensity change between the two blade geometries match the experimental findings. For the erosion zone, we observe a general alignment in between experiment and numerical solution for all indicators and geometries. There is, however, a notable narrowness of the predicted affected region and a clear shift of the peak in the upstream direction. The width of the predicted erosion action is determined by the width of the unsteady cavitating region. At $\sigma_{num} = 0.585$ for both geometries, the time-resolved simulation produced a cavity with smaller variations in length than recorded experimentally. If we consider the baseline case, all tested erosion models, except for the Mouvanal approach, predict material loss between $x/chord = 0.35$ and $x/chord = 0.4$. This corresponds to the zone of highest pressure and volume fraction variation (see Fig. 15). The Mouvanal technique is the only one that produces an erosion zone that begins at $x/chord = 0.4$ and ends at $x/chord = 0.46$ with a peak that matches experimental data. The specificity of this approach is that it is not the immediate pressure or volume fraction and their rate of change that is taken into consideration, but whether conditions spanning previous time steps are met. This produces a delay in activation of cavitation erosion compared to the other methods. It is also worth noting that for the shape of the erosion distribution, all produce an abrupt peak centered at the closure point rather than the rounded experimental curve. The exception, here again, is the Mouvanal approach.

In terms of differences across designs, we pick up the drop in erosion aggressiveness for the design case over the baseline for most of the tested models except for two, which indicate an increase in the intensity of collapse events. These are the Peters *et al.* (2015) approach, based on jet velocity and so driven by $\sqrt{p - pv}$, and Nohmi *et al.* (2009) second form, also determined by $p - pv$. This suggests that using the pressure rather than its time variation—as is done by Li *et al.* (2014)—or without conditional checks for condensation—as in Mouvanal *et al.* (2018)—does not deliver an accurate metric for cavitation erosion. As for the best performing erosion models in terms of drop in aggressiveness, it is the Mouvanal *et al.* (2018) technique that delivers the best match. Indeed, the calculated reduction factor from baseline to design for peak erosion is of approximately 0.36, a value comparatively close to the 0.41 factor for experimental data.

VI. CONCLUSION

This paper presented the experimental study of two cavitating hydrofoil geometries: a conventional, smooth baseline blade and a blade generated using the inverse design approach under cavitating conditions in such a way that the pressure jump at cavity closure was smoothed down, while maintaining the same overall pressure rise. A key feature of the design blade is the suction side surface kink at the location of cavity closure and the ensuing wavy pressure distribution. Two experiments were conducted here: i. a flow characterization analysis aimed at studying the pressure profile and blade cavitation behavior, and ii. a cavitation erosion intensity comparison to measure the effects of the design.

For the flow characterization analysis, the flow field was evaluated by means of surface pressure readings and visual recordings of blade cavitation. The reliability of the experimental rig was validated by checking that non-cavitating pressure measurements were in agreement with the distributions predicted numerically for both tested cases. Non-cavitating runs also confirmed that the wavy suction side distribution of the design case did not adversely perturb the flow field: the boundary layer remained attached throughout the kink region.

Comparing cavitating flow characterization results for the two blades confirmed the similarity in inception conditions and cavity growth rate for the baseline and the inverse design blade. However, the study revealed a significant difference in the aspect of cavitation between the two cases. For identical conditions, the design blade produced a thinner, more stable cavity with a substantially smaller bubbly region at cavity closure.

The erosive power experiment consisted in using the paint removal approach to measure cavitation aggressiveness. Erosion results were obtained after 15 h of exposure at $\sigma = 0.73$ (or for a closure location of $x/chord \approx 0.4$) and processed through imaging techniques to generate streamwise aggressiveness profiles for each blade.

The main goal of the experimental erosion analysis was to assess the impact of the pressure jump smoothing design strategy laid out in Nahon *et al.* (2021). The comparative analysis revealed a clear disparity in erosion patterns: for the baseline, the paint layer was fully eroded over a wide chordwise region ($x/chord = 0.3$ to $x/chord = 0.5$), while for the inverse design blade, the painted surface was only speckled in a narrow region ($x/chord = 0.4$ to $x/chord = 0.5$). This presents a clear validation of the design approach, which produces a blade with a cavitation pattern that is more stable, reduces bubbly mixing at cavity closure, and above all cuts down erosion aggressiveness.

In this work, we also compared experimental erosion patterns to patterns predicted numerically using four different modeling approaches. It was found that all numerical models matched the experimental results in terms of location but consistently under-evaluated the spread of erosion. Out of the tested techniques, the method that fared best was the Mouvanal *et al.* (2018) indicator, which correctly captured the change in erosion intensity across the two blades.

The experimental results presented here confirm that the original hypothesis, that is, smoothing the pressure jump at cavity closure using the inverse design method to reduce cavitation aggressiveness, does indeed lead to a reduction in erosion without any performance penalties. This is a major finding, which, when extended to 3D, could lead to a paradigm shift in the design of hydraulic machines: rather than designing for delayed cavitation onset at the expense of hydraulic efficiency, one can now design high efficiency compact machines with equal or extended operating life times.

ACKNOWLEDGMENTS

This work was funded by Ebara Corporation, Japan.

AUTHOR DECLARATIONS

Conflict of Interest

The authors have no conflicts to disclose.

Author Contributions

Jeremy Nahon: Conceptualization (equal); Formal analysis (equal); Investigation (equal); Writing – original draft (equal). **Mehrdad**

Zangeneh: Conceptualization (equal); Funding acquisition (equal); Supervision (equal). **Tomoki Tsuneda:** Investigation (equal); Validation (equal). **Motohiko Nohmi:** Conceptualization (equal); Formal analysis (equal); Methodology (equal). **Hiroyoshi Watanabe:** Methodology (equal); Project administration (equal); Supervision (equal). **Akira Goto:** Conceptualization (equal); Methodology (equal); Project administration (equal).

DATA AVAILABILITY

The data that support the findings of this study are available from the corresponding author upon reasonable request.

REFERENCES

Avellan, F. and Dupont, P., "Cavitation erosion of the hydraulic machines: Generation and dynamics of erosive cavities," in *Proceedings of the 14th IAHR Symposium on Hydraulic Machinery: Progress within Large and High Specific Energy Units* (International Association For Hydraulic Research, 1988), pp. 725–738.

Blake, J., "The Kelvin impulse: Application to cavitation bubble dynamics," J. Aust. Math. Soc. Ser. B **30**(2), 127–146 (1988).

Bonaiuti, D., Zangeneh, M., Aartojarvi, A., and Eriksson, J., "Parametric design of a waterjet pump by means of inverse design, CFD calculation and experimental analyses," J. Fluids Eng. **132**, 031104 (2010).

Brennen, C. E., *Hydrodynamics of Pumps* (Oxford University Press/Concepts EDI, 2011).

Brennen, C. E., *Cavitation and Bubble Dynamics* (Oxford University Press, New York, 2013).

Chan, W. K., "Correlation between cavitation type and cavitation erosion in centrifugal pumps," Int. J. Heat Fluid Flow **11**, 269–271 (1990).

Ducoin, A., Huang, B., and Young, Y. L., "Numerical modelling of unsteady cavitating flows around a stationary hydrofoil," Int. J. Rotating Mach. **2012**, 215678 (2012).

Dular, M., Bachert, B., Stoffel, B., and Širok, B., "Relationship between cavitation structures and cavitation damage," Wear **257**, 1176–1184 (2004).

Dular, M., Stoffel, B., and Širok, B., "Development of a cavitation erosion model," Wear **261**, 642–655 (2006).

Fortes Patella, R. and Reboud, J. L., "A new approach to evaluate the cavitation erosion power," J. Fluids Eng. **120**, 335 (1998).

Fukaya, M., Tamura, Y., and Matsumoto, Y., "Prediction of cavitation intensity and erosion area in centrifugal pump by using cavitating flow simulation with bubble flow model," J. Fluid Sci. Technol. **5**, 305–316 (2010).

Gulich, J. F., *Centrifugal Pumps*, 2nd ed. (Springer, Heidelberg, 2010).

Hammitt, F. G., "Observations on cavitation damage in a flowing system," J. Basic Eng. **85**, 347 (1963).

Hofmann, M., Stoffel, B., Friedrichs, J., and Kosyna, G., "Similarities and geometrical effects on rotating cavitation in two scaled centrifugal pumps," in *Fourth International Symposium on Cavitation*, Pasadena, CA, 2001.

Kato, H., Konno, A., Maeda, M., and Yamaguchi, H., "Possibility of quantitative prediction of cavitation erosion without model test," J. Fluids Eng. **118**, 582 (1996).

Li, Z., Pourquie, M., and van Terwisga, T., "Assessment of cavitation erosion with a URANS method," J. Fluids Eng. **136**, 041101 (2014).

Lohrberg, H., "Messung und aktive kontrolle der erosiven aggressivität der kavitation in turbomaschinen," Ph.D. thesis (Technical University of Darmstadt, Darmstadt, Germany, 2001).

Monteith, J. and Unsworth, M., *Principles of Environmental Physics: Plants, Animals, and the Atmosphere* (Academic Press, 2013).

Mouvanal, S., Chatterjee, D., Bakshi, S., Burkhardt, A., and Mohr, V., "Numerical prediction of potential cavitation erosion in fuel injectors," Int. J. Multiphase Flow **104**, 113–124 (2018).

Nahon, J., "Novel blade design strategy to control the erosion aggressiveness of cavitation," Ph.D. thesis (University College London, London, United Kingdom, 2020).

Nahon, J., Zangeneh, M., Nohmi, M., and Watanabe, H., "Numerical investigation on the effect of blade loading on unsteady sheet cavitation patterns," in *Proceedings of the ASME-JSME-KSME 2019 8th Joint Fluids Engineering Conference*, San Francisco, CA, 28 July–1 August 2019 (ASME, 2019).

Nahon, J., Zangeneh, M., Nohmi, M., Watanabe, H., and Goto, A., "A robust inverse design solver for controlling the potential aggressiveness of cavitating flow on hydrofoil cascades," Int. J. Numer. Methods Fluids **93**, 2291–2310 (2021).

Nohmi, M., Goto, A., Iga, Y., and Ikohagi, T., "Cavitation CFD in a Centrifugal Pump," in Fifth International Symposium on Cavitation (CAV2003), Osaka, 2003.

Nohmi, M., Ikohagi, T., and Iga, Y., "Numerical prediction method of cavitation erosion," in *ASME Fluids Engineering Conference* (ASME, 2009), pp. 1139–1145.

Ochiai, N., Iga, Y., Nohmi, M., and Ikohagi, T., "Numerical prediction of cavitation erosion intensity in cavitating flows around a Clark Y 11.7% hydrofoil," J. Fluid Sci. Technol. **5**, 416–431 (2010).

Pereira, F., Avellan, F., and Dupont, P., "Prediction of cavitation erosion: An energy approach," J. Fluids Eng. **120**, 719 (1998).

Peters, A., Sagar, H., Lantermann, U., and el Moctar, O., "Numerical modelling and prediction of cavitation erosion," Wear **338–339**, 189–201 (2015).

Petkovšek, M. and Dular, M., "Simultaneous observation of cavitation structures and cavitation erosion," Wear **300**, 55–64 (2013).

Sagar, H. and el Moctar, O., "Dynamics of a cavitation bubble near a solid surface and the induced damage," J. Fluids Struct. **92**, 102799 (2020).

Shima, E. and Kitamura, K., "Parameter-free simple low-dissipation AUSM-family scheme for all speeds," AIAA J. **49**, 1693–1709 (2011).

Shimada, M., Matsumoto, Y., and Kobayashi, T., "Dynamics of the cloud cavitation and cavitation erosion," Trans. Jpn. Soc. Mech. Eng., Ser. B **65**, 1934–1941 (1999).

Tiow, M., Matsumoto, Y., and Kobayashi, T., "Application of a three-dimensional viscous transonic inverse method to NASA rotor 67. Proceedings of the Institution of Mechanical Engineers, Part A," J. Power and Energy, **261**(3), 243–256 (2002).

Yu, W. T. and Zangeneh, M., "Preliminary discussion for improving cavitating flow around hydrofoil by punching," Procedia Eng. **31**, 261–266 (2012).

Zangeneh, M., Goto, A., and Takemura, T., "Suppression of secondary flows in a mixed-flow pump impeller by application of three-dimensional inverse design method: Part 1—Design and numerical validation," J. Turbomach. **118**, 536 (1996).

Zwart, P. J., Gerber, A. G., and Belamri, T., "A two-phase flow model for predicting cavitation dynamics," in *International Conference on Multiphase Flow* (ICMF, 2004), p. 152.